Technical Report

Effect of Ripple Loads on Stress-Corrosion Cracking in Structural Steels

Submitted to:

Mr. Charles E. Smith
Research Program Manager
Offshore Minerals Management
Technology Assessment and Research Branch
Minerals Management Service
381 Elden Street, MS 4700
Herndon, VA 22070-4817

Submitted by:

P.S. Pao, and R.A. Bayles

Environmental Effects Branch
Materials Sciences and Technology Division
NAVAL RESEARCH LABORATORY
Washington, D.C. 20375-5343

Report No. NRL ser 6310/003
May 30, 1995

TABLE OF CONTENTS

Technical Report

Effect of Ripple Loads on Stress-Corrosion Cracking in Structural Steels

P.S. Pao and R.A. Bayles

Naval Research Laboratory, Washington, DC 20375-5343

ABSTRACT

If very small amplitude cyclic (or "ripple") loads perturb an otherwise constant load condition in an aggressive environment, life prediction based solely on the static stress-corrosion cracking threshold (K_{ISCC}) may prove nonconservative, as the ripple-load effect may produce fracture in a structural alloy at stress-intensity levels less than 50% of K_{ISCC}. Ripple-load cracking has been successfully treated as an extreme case of corrosion fatigue. A predictive framework for such ripple-loading effects (RLE) is developed from concepts and descriptors used in SCC and corrosion fatigue characterization. The proposed framework is capable of defining critical conditions required for the occurrence of RLE and predicting time-to-failure curves. A new threshold parameter, K_{IRLC}, which defines the threshold stress-intensity factor below which ripple-load cracking will not occur, is identified to ensure fail-safe life even in the presence of the ripple effect. A "window" for ripple-load cracking susceptibility, bounded by K_{IRLC} and K_{ISCC}, defines the critical conditions for ripple-load cracking. The predicted ripple-load cracking time-to-failure curves agree well with experimental measurements. From studies of several steels, it is found that 5Ni-Cr-Mo-V steel (HY-130) and TLP tendon pipe steel, both of which exhibit good stress-corrosion cracking resistance, are prone to degradation by the ripple effect.

KEY WORDS : crack propagation, ripple-load cracking, stress-corrosion cracking, corrosion fatigue, steels, tension leg platform

1.0 INTRODUCTION

Stress-corrosion cracking (SCC) is a cracking process caused by the conjoint action of stress and a corrodent [1]. Conceptually, SCC will occur if a sensitive material is exposed to a corrosive environment under sufficient stress for a sufficient length of time. For a structural material which contains a crack or crack-like defect, the resistance to SCC is normally evaluated in terms of the fracture mechanics parameter, K_{ISCC}, the threshold stress-intensity factor below which crack extension will not occur. The measurement of K_{ISCC} and its application to design of structures for the marine environment commonly presumes sustained or constant load conditions. However, in the real world, a constant load condition is rarely attainable. For example, the loading profiles experienced by offshore platform structures most likely involve the superposition of relatively small amplitude cyclic load perturbations on a substantially larger constant load. Though such perturbations might at first glance seem virtually insignificant on the basis of their amplitude, preliminary study has shown that their effect, described as the "ripple effect" by Speidel [2], can be sizable. An example of a ripple-load profile is schematically shown in Fig. 1. Recent work at the Naval Research Laboratory on steels, titanium, and aluminum alloys has suggested that the presence of such ripple loads can significantly reduce the apparent SCC threshold and can shorten the life of a structure [3-8]. Others have also observed that small fluctuating loads may produce SCC at significantly lower stresses than those required under purely static loads [9-18]. Thus, a design based solely on the static K_{ISCC} without proper consideration of the ripple-load effect (RLE), may be nonconservative.

The objective of this study is to develop an understanding of RLE and the framework required for the prediction of RLE. First of all, RLE is investigated in two different classes of steels: the medium strength, high toughness 5Ni-Cr-Mo-V steel and tension leg platform (TLP) tendon pipe steel (0.06C, 0.2Si, 0.21Cu, 0.2Ni, Bal Fe), and the high strength, low toughness AISI 4340 steel. Secondly, the critical conditions required for a material to exhibit RLE in marine

environment are defined and quantitative prediction of the maximum extent of degradation by RLE is presented. A new ripple-load cracking threshold, K_{IRLC}, which marks the onset of ripple-load crack growth, has been devised and is offered as an alternative design parameter to represent the upper bound of the design limit. And finally, the quantitative predictive methodology for time-to-failure curves associated with ripple-load cracking is offered for a given combination of material and loading conditions.

2.0 MATERIALS AND EXPERIMENTAL PROCEDURES

2.1 Materials

The three steels studied in this investigation were TLP tendon pipe steel, 5Ni-Cr-Mo-V steel, and AISI 4340 steel. The chemical analysis and the tensile properties are given in Tables 1 and 2, respectively.

2.2 Ripple-Load "Direct Experiments"

Figure 2 shows the design of the "direct experiment" used to evaluate the effect of ripple loading on steels. The apparatus is a cantilever bend load frame, modified with a motorized cam to superimpose a small oscillating load onto the dead-weight load.

The specimens were fatigue-precracked in air, then the environment cup was sealed to the specimen. After the specimen was mounted in the load frame, the cup was filled with 3.5% NaCl solution. After 24 hours a dead-weight load was gradually applied while a crack mouth opening gage was used to determine, by means of compliance, the crack depth. Enough load was then applied to produce the desired K_{max}. The eccentric cam and spring apparatus was set up to cyclically reduce the load by the desired amount - in the case described here 10% (R=0.90) of the dead-weight load. The cam motor was switched on to begin the experiment. A cyclic frequency of 0.1 Hz (6 cpm) was used to simulate ocean wave motion. Evaporation losses were made up with distilled water as needed and the saltwater was replaced weekly.

For 5Ni-Cr-Mo-V and AISI 4340 steel, time-to-failure data under SCC and ripple-load conditions were determined using precracked cantilever-beam specimens of length L=400 mm, width W=50.8 mm and thickness B=25.4 mm, with an initial (normalized) crack length of a/W=0.5 and sidegrooves of depth 1.25 mm per side. All tests were conducted at ambient temperature. The

AISI 4340 steel was tested at the freely corroding potential. The 5Ni-Cr-Mo-V steel was tested at a potential of approximately -1.0 V obtained by coupling to zinc anodes.

2.3 Corrosion-Fatigue Tests

For TLP tendon pipe steel, fracture mechanics type specimens were machined from the base metal region and from the weld region of 609.6 mm (24") O.D. TLP tendon pipe with a wall thickness of 20.6 mm. For weld region specimens, as shown in Fig. 3, the starter notch was located at the center of the fusion zone and the intended crack-growth direction was parallel to the welding direction (circumferentially). Time-to-failure data under SCC and ripple-load conditions were determined in the weld region and in the base metal using precracked compact-tension specimens of width W=31.5 mm and thickness B=15.1 mm, with sidegrooves of depth 0.8 mm per side. To simulate a ripple-load condition and to measure threshold levels of stress-intensity range directly, precracked specimens were cyclically loaded using a corrosion-fatigue apparatus which is shown schematically in Fig. 4. Tests were conducted at either room temperature (20 °C) or 3 °C (to simulate deep water temperature) in a 3.5% NaCl solution with a stress ratio (minimum: maximum) of R = 0.90, a haversine waveform, and a cyclic frequency of 5 Hz. SCC thresholds were determined in the 3.5% NaCl solution using constant load cantilever bend bar tests. The TLP tendon pipe steel was tested at a potential of -0.9 V. Crack lengths were determined using a compliance related CMOD technique. Details of the experimental procedures have been published elsewhere [3, 6-8, 19].

The method described here uses corrosion-fatigue data from one specimen, typically obtained in a few weeks, to predict the complete ripple-load curve between K_{ISCC} and K_{IRLC}. The direct experiment approach required many experiments and, for steels, test durations of up to many years.

3.0 RESULTS

3.1 Analysis of the Ripple-Load Effect

In this investigation, ripple-load cracking is approached as an extreme case of corrosion-fatigue crack growth behavior at very high stress ratios. The desired predictive framework for RLE necessarily involves the interface between SCC and corrosion-fatigue behavior. Thus, the analysis begins with consideration of the relationship between the small amplitude stress-intensity range associated with ripple loading, ΔK, the threshold for corrosion fatigue, ΔK_{th}, the maximum stress-intensity, K_{max}, and K_{ISCC}.

3.1.1 Critical Conditions (for susceptibility)

To define the critical conditions required for a material to exhibit a RLE in marine environment, consider first of all the nature of the interface between stress-corrosion cracking and corrosion fatigue. In Fig. 5, the SCC resistance is indicated by the "static" loading curve, wherein the level of K represents the initial value of stress-intensity factor associated with a precracked specimen (or structure) which is subjected to a constant load. However, if this constant load is superposed with a "ripple" or small-amplitude cyclic load --- as in the schematic of Fig. 1, then, for a material exhibiting susceptibility to a RLE, cracking resistance appears to be degraded to levels significantly below the "static" threshold K_{ISCC}, as in Fig. 5. There, the K-level plotted for the "ripple" curve is actually K_{max}^{RL}, the maximum level of K in the ripple-load cycle.

A structure stressed above K_{ISCC} and under a sustained load is expected to fail by a stress-corrosion cracking mechanism. In this study, our attention was focused on the regime below K_{ISCC} where propagation of existing cracks and failure are not expected under a constant load condition. Thus, with the presence of small ripples superimposed on a large sustained load, cf. Fig.

1, the maximum stress intensity in the ripple-load cycle, K_{max}^{RL}, was equal to or less than K_{ISCC}. That is, the first condition for ripple-load cracking can be set as:

$$K_{max}^{RL} \leq K_{ISCC} \qquad (1)$$

Next, from corrosion-fatigue considerations, crack propagation is not going to take place during ripple loading unless ΔK^{RL} in the ripple cycle equals to or exceeds ΔK_{th} or:

$$\Delta K_{th} \leq \Delta K^{RL} \qquad (2)$$

or $$\frac{\Delta K_{th}}{1-R} \leq K_{max}^{RL} \qquad (2a)$$

Thus, a new parameter, K_{IRLC}, the ripple-load cracking threshold below which ripple-load cracking does not occur, can be defined as:

$$K_{IRLC} = \frac{\Delta K_{th}}{1-R} \qquad (3)$$

Combining (1), (2a), and (3), the conditions for a material to exhibit a ripple-load cracking are:

$$K_{IRLC} \leq K_{max}^{RL} \leq K_{ISCC} \qquad (4)$$

3.1.2 Maximum Extent of Degradation

Relation (4) is schematically illustrated in Fig. 6. The ripple effect region, whose upper bound is the stress-corrosion cracking threshold, K_{ISCC}, and whose lower bound is the ripple-load cracking threshold, K_{IRLC}, defines a "window of susceptibility" in which the ripple-load effect

would be anticipated. The wider the window the more susceptible the material is to ripple-load cracking. In the extreme case, where K_{IRLC} approaches K_{ISCC}, the susceptibility window vanishes and no ripple-load effect is expected.

If one considers the difference between the threshold for ripple-load cracking, K_{IRLC}, and K_{ISCC}, then the maximum extent of ripple-load degradation can be defined as:

$$\% \text{ degradation} = (1 - K_{IRLC} / K_{ISCC}) \times 100 \tag{5}$$

On the other hand, if conditions of relation (4) are not met, a material will not exhibit susceptibility to a RLE.

3.1.3 Quantitative Prediction of Time-to-Failure (t_f) Curves

Though the typical logarithmic corrosion-fatigue crack-growth rate curve may well exhibit a more complex shape than shown in the schematic of Fig. 7, nevertheless, it can be approximated in piecewise fashion with power-law segments,

$$\frac{da}{dN} = C_j(\Delta K)^{m_j} \tag{6}$$

Thus, the total number of cycles to propagate a crack to failure follows the piecewise integration (over j segments) as [20]:

$$(N_p)_j = \int_{(a_i)_j}^{(a_f)_j} \frac{da}{C_j\left[(1-R)\ P_{max}\ f(a, Q)\right]^{m_j}} \tag{7}$$

where P is load and f(a,Q) is a function of crack length (a) and structural geometry (Q). Since time-to-failure is simply given by:

$$t_f = \frac{\sum_i (N_p)_j}{\nu} \tag{8}$$

where ν is the cyclic frequency, then t_f can be estimated as:

$$t_f = \frac{1}{\nu} \sum_j \int_{(a_i)_j}^{(a_f)_j} \frac{da}{C_j \left[(1-R)\ P_{max}\ f(a,Q) \right]^{m_j}} \tag{9}$$

Though in certain cases f(a,Q) is sufficiently simple to permit direct integration of Eq. 9 --- such as in the case of a center-cracked tension panel, in general, a numerical integration will facilitate computation.

3.2 Ripple-Load Cracking in 5Ni-Cr-Mo-V Steel

Ripple-load cracking and SCC experimental results obtained on the 5Ni-Cr-Mo-V steel are shown in Fig. 8. For tests involving ripple-loading, initial K_I corresponds to the maximum stress intensity factor in the loading cycle, as shown in Fig. 1.

For the 5Ni-Cr-Mo-V steel, a static K_{ISCC} was established at 110 MPa $\sqrt{m}$ (100 ksi $\sqrt{in.}$) based upon multiple long-term tests exceeding 10,000 hours. Ripple-loading data were obtained at R values of 0.90, 0.95 and 0.975, using "direct experiments" as outlined in Section 2.2. Except for R = 0.975, all ripple-loading conditions resulted in reduced values of time-to-failure and lower

apparent threshold values. That is, 5Ni-Cr-Mo-V steel is susceptible to RLE under R=0.95 and R=0.90 conditions. For R = 0.975, the apparent threshold equaled the static K_{ISCC}. For R = 0.95 and 0.90, the apparent thresholds were 80 and 44 MPa$\sqrt{m}$ (74 and 40 ksi$\sqrt{in.}$), respectively. As we will see in the upcoming analysis, these thresholds estimated from 4000-hour direct exposures are nonconservative.

As shown in Fig. 8, ripple-loading has a strongly deleterious effect in 5Ni-Cr-Mo-V steel on both apparent threshold levels and on time-to-failure [3]. The apparent threshold levels and time-to-failure under ripple-loading conditions can be analytically predicted from Eqs. 3 and 9, provided that the threshold stress-intensity range and the corrosion-fatigue crack-growth rate corresponding to the particular stress ratio in a similar environment can be established. Vosikovsky has conducted a systematic investigation on the effect of stress ratio on the fatigue crack growth rate in 3.5% NaCl solution on a 5Ni-Cr-Mo-V steel very similar to the one used in the present study [21]. A ΔK_{th} value for R=0.90 and ν=0.1Hz is reported to be 3.10 MPa$\sqrt{m}$. ΔK_{th} values for R=0.95 and 0.975 can be estimated by extrapolation of Vosikovsky's analytical expression [21] and are approximately 2.95 and 2.875 MPa$\sqrt{m}$, respectively. Based on these measurements and Eq. 3, the threshold values under ripple-loading conditions of R=0.90, 0.95, and 0.975 are analytically predicted to be 31, 59, and 115 MPa$\sqrt{m}$, respectively. These predicted values are then compared in Table 3 with the experimentally deduced apparent threshold values (from Fig. 8). As shown in Table 3, under a very small ripple-loading of R=0.975, the predicted threshold value is greater than K_{ISCC}. Thus, according to Eq. 4, no RLE is expected as it is in agreement with the experimental results (Fig. 8). For ripple-loading conditions of R=0.90 and 0.95, the predicted threshold values are significantly lower than their experimentally determined counterparts. That is, threshold values based on 4000-hour ripple-load cracking tests are nonconservative. On the other hand, this does not indicate a significant discrepancy between theory and experiment. Rather, as will be shown next, our analysis indicates that the 4000-hr test duration is inappropriately too short.

The time-to-failure curve can be predicted by numerical integration of Eq. 9, provided the corrosion-fatigue crack growth rate curve is established. Again Vosikovsky's crack growth rate data at R=0.90 is used for numerical integration, relative to the identical cantilever bend-bar geometry used in the experimental work. The procedure is quite straight-forward and involves the fitting of power-law equations in different regions of the crack growth rate data and the subsequent integration using Eq. 9. The predicted time-to-failure curve based on Vosikovsky's data at R=0.90 is presented and compared with the experimental data in Fig. 9. As shown in Fig. 9, excellent agreement between predicted curve and actual experimental data is achieved. This agreement confirms the validity of approaching ripple-load cracking as an extreme case of corrosion-fatigue cracking. Each of the open circles indicates a separate direct experiment. The longest direct experiment was run for 8000 hours and failure of the specimen was not observed. The prediction indicates that the true threshold value for ripple loading, K_{IRLC}, is substantially lower, but a direct experiment duration on the order of 30,000 hours (~3.5 years)would be required to confirm this. Thus, a 4000-hr test for ripple-load threshold is inappropriately short in the case of this alloy.

3.3 Ripple-Load Cracking in AISI 4340 Steel

For the AISI 4340 steel, a long-term static K_{ISCC} value was established at 33 MPa$\sqrt{m}$ (30 ksi$\sqrt{in.}$) [3]. As shown in Fig. 10, superimposed on these K_I vs. time-to-failure data curve are two ripple-loading tests with R = 0.90 (largest ripple). To define ΔK_{th}, corrosion fatigue tests were performed in the present study at R=0.90 on AISI 4340 steel specimens in 3.5% NaCl solution. The ΔK_{th} at R=0.90 was found to be 3.3 MPa$\sqrt{m}$. Substituting this threshold value in Eq. 3, then the threshold level of K, below which ripple-load cracking will not occur, is estimated to be 33 MPa$\sqrt{m}$, which is identical to K_{ISCC} of the AISI 4340 steel. According to the framework predictions of Eq. 4, a ripple-load effect will not occur. As is shown in Fig. 10, this is exactly what happens to AISI 4340 steel under ripple loading (R=0.90) [3]. In other words, AISI 4340 steel is

not susceptible to RLE even at R = 0.90. Thus, the nonsusceptibility of AISI 4340 steel to RLE can be accurately predicted with the proposed framework.

3.4 Ripple-Load Cracking in TLP Tendon Pipe Steel

3.4.1 Microstructure in the Base Metal and Weld Region

The fine base metal microstructure of TLP tendon pipe steel is shown in Fig. 11. The weld region microstructure is shown in Fig. 12. As shown in Fig. 12, the center of this multi-pass weld region (fusion zone), which is marked by a pair of notches, consists of very large columnar grains (Fig. 13). The microhardness across the weld region was also obtained and is shown in Fig. 14. The microhardness and thus the strength in the center fusion zone is substantially higher than that in the base metal region. The above observation is typical for the medium strength carbon steels.

3.4.2 Ripple-Load Cracking in the Base Metal and in Weld Region

3.4.2.1 At 20 °C

The ripple-load crack growth kinetics of the base metal and the weld region in a 3.5% aqueous NaCl solution at ambient temperature with a ripple amplitude equal to 5% of the sustained load (R=0.90) are compared in Fig. 15. As shown in Fig. 15, the ripple-load crack growth data exhibit a sigmoidal pattern similar to those obtained at lower stress ratios except in the ripple loading case where the transition from the slow and near-threshold crack growth to the instability spans only a few stress-intensity factors. Figure 15 indicates that the base metal and the weld region have similar crack growth rates at any given stress-intensity and may have identical ΔK_{th}. That is, crack tip microstructure has little effect on the fatigue crack growth characteristics for the TLP tendon pipe steel at R = 0.90. The fatigue crack growth threshold stress-intensity factor range

(ΔK_{th}) is estimated to be 3.15 MPa$\sqrt{m}$ for both base metal and weld regions in a 3.5% NaCl solution at a stress ratio of 0.90. According to Eq. 3, the ripple-load cracking threshold, K_{IRLC}, would equal 31.5 MPa$\sqrt{m}$. That is, below this ripple-load cracking threshold, crack growth in a 3.5% NaCl solution is not expected even under ripple loading with a ripple amplitude equal to 5% of the sustained load. Above K_{IRLC}, subcritical cracks would grow under ripple loading conditions.

Values of K_{ISCC} for the base metal and weld regions determined by constant load cantilever bend bar tests in the 3.5% NaCl solution are estimated to be higher than 78 but lower than 93 MPa$\sqrt{m}$. In the subsequent ripple-load cracking analysis of TLP tendon pipe steel, a lower and more conservative 78 MPa$\sqrt{m}$ is used as the K_{ISCC} of this steel.

The effect of ripple loading on SCC can be better illustrated by integrating numerically the fatigue data shown in Fig. 15 and by comparing K_{IRLC} with K_{ISCC} directly in the same plot. Figure 16 shows the time-to-failure versus applied stress-intensity curves under ripple loading conditions for both base metal and weld regions of TLP tendon pipe steel, obtained by piecewise integration of the fatigue data shown in Fig. 15. As shown in Fig. 16, there are three regions which are separated by K_{ISCC} and K_{IRLC}. In Region 3, the maximum applied stress intensity experienced during ripple loading is higher than either K_{ISCC} or K_{IRLC}. In this region, cracks will grow by both fatigue and stress-corrosion cracking mechanisms and a superposition model was developed to address the cracking phenomena [22]. Since stress-corrosion crack growth in steels is well recognized, structural failures in this region are less likely because marine structural designers will take it into consideration when they design a new structure. On the other hand, in Region 1, the maximum applied stress intensity is lower than both K_{ISCC} and K_{IRLC}. Under such a loading condition, existing cracks in the structure will be non-propagating, even under ripple loads.

Region 2, which is upper-bounded by K_{ISCC} and lower-bounded by K_{IRLC}, is more interesting. Since the maximum applied stress intensity is lower than K_{ISCC}, stress-corrosion cracking is not expected. However, the applied stress intensity is higher than K_{IRLC} and cracks will grow under ripple-load conditions. As shown in Fig. 16, in the presence of ripple loads (R=0.90), the K_{IRLC} of TLP tendon pipe steel in 3.5% NaCl solution is 31.5 MPa$\sqrt{m}$. This represents a ripple-load degradation of 60% when compared to K_{ISCC}. Thus, Region 2 can be termed the ripple-load cracking susceptible region. Because of the possibility of ripple-load cracking, it is suggested that K_{IRLC} (which is less than half of K_{ISCC} for TLP tendon pipe steel investigated) be incorporated into the design process whenever a structure is designed to support a large sustained load with possible small load perturbations. One should be particularly careful with the SCC-resistant alloys because there is more room for a drop from their high K_{ISCC} and because they are more likely to be selected for use in potential ripple loading conditions. Otherwise, a design based only on the sustained load K_{ISCC} would be nonconservative in this region.

3.4.2.2 At 3 °C

To simulate deep water temperature conditions, ripple-load crack growth kinetics were determined for base metal at 3 °C under ripple loading (R=0.90) in 3.5% NaCl solution. Figure 17 shows the comparison of crack growth kinetics obtained at 3 °C and 20 °C. As shown in Fig. 17, in the intermediate ΔK region, the crack growth rate under ripple loading at 3 °C is about two times faster than that at 20 °C. In the near threshold region, however, crack growth rates and the threshold stress intensity factor ranges, ΔK_{th}, at these two temperatures are almost identical. Therefore, the ripple load cracking threshold, K_{IRLC}, at 3 °C for this TLP tendon pipe steel is the same as that for 20 °C.

Figure 18 shows the predicted time-to-failure versus applied stress-intensity curve under ripple loading conditions at 3 °C for TLP tendon pipe steel, obtained by piecewise integration of the

fatigue data shown in Fig. 17. Because the crack growth rates are higher at 3 °C, the failure time at similar stress intensity is slightly shorter when compared to that obtained at 20 °C. As shown in Fig. 18, the K_{IRLC} under R = 0.90 ripple loading at 3 °C is about 60% lower than the K_{ISCC} (otained at 20 °C).

4.0 DISCUSSION

It is useful to elaborate somewhat on a number of points related to the predictive methodology offered in this investigation. Table 3 clearly establishes that materials which exhibit greater SCC resistance under static load conditions are far more susceptible to ripple-load degradation. In other NRL studies, we also have demonstrated that in each of the three engineering material families, highly SCC-resistant alloys are more prone to ripple-load degradation than less SCC-resistant alloys [3-8]. The more SCC-resistant 5Ni-Cr-Mo-V steel and TLP tendon pipe steel experience reductions of more than 50% in apparent K_{ISCC} when they are subjected to a ripple-load condition. On the contrary, the less SCC-resistant AISI 4340 steel exhibits no ripple-load degradation. The significance of this finding is obvious, at least phenomenologically, as a structure designed to take advantage of the high K_{ISCC} of a highly SCC-resistant material may fail unexpectedly if ripple-load conditions exist. To circumvent this problem, it is suggested that the possibility of ripple loading in the operating environment should be considered early in the design process, and if a ripple condition indeed does exist, the ripple-load cracking threshold, K_{IRLC}, should be used instead of the static K_{ISCC} to determine the allowable stress and inspection intervals.

Secondly, it is significant to note that the ripple effect depends strongly on the size or amplitude of the ripple loads. The larger the ripple-load amplitude, the more damaging the ripple effect. As the fatigue crack growth threshold, ΔK_{th}, varies with the stress ratio, R, the ripple-load cracking threshold, K_{IRLC}, correspondingly varies with R according to Eq. 3. Thus, while a material may exhibit substantial ripple-load degradation with larger amplitude ripple loading, the same material may show less or even no ripple-load degradation if the existing ripples are smaller. Ripple load cracking tests at various ripple sizes on 5Ni-Cr-Mo-V steel clearly demonstrate this important point. A separate study had also shown that extremely small ripple loads (smaller than

2% of the sustained load) had no effect on the stress-corrosion cracking resistance of peakaged TIMETAL 21S [23].

Material sensitivities to ripple-load degradation, as defined by the contrast in results found in this investigation, pose an intriguing dilemma to the engineer who must select structural materials for performance in a specific environment. It is clearly disconcerting to the engineer to observe that materials which exhibit the greater SCC resistance under static load condition are the same materials which often exhibit the greater sensitivity to ripple-load degradation. For the specific materials and conditions examined in this work, the more SCC-resistant materials, 5Ni-Cr-Mo-V steel and TLP tendon pipe steel, are more prone to ripple-load degradation than the less SCC-resistant high strength AISI 4340 steel. Even though materials with superior SCC resistance exhibit larger ripple load degradation, there are indications, as shown in Table 3, that their K_{IRLC} values are close to their less SCC-resistant counterpart. Thus, SCC-resistant materials may still be the material of the choice even with the presence of ripple loading. However, in such instances, the ripple-load cracking threshold K_{IRLC} should be used for the conservative design of structural components.

A few words are also in order regarding the time-to-failure curves. It is significant to note that although the high stress ratio corrosion fatigue data required for the prediction of time-to-failure via Eq. 9 are difficult to obtain from the literature, they may be readily acquired through automated test methods [24]. The predictive framework thus permits the saving of the much greater time and expense associated with the direct experimental determination of such time-to-failure curves, reducing the testing time from years to a couple of months --- with much of that time spent determining near-threshold behavior.

Finally, ripple-load cracking characteristics can be affected by mechanical and environmental parameters. However, many of these are not adequately understood. While this study shows that ripple loading at R=0.90 causes substantial ripple-load degradation of TLP tendon

pipe steel and 5Ni-Cr-Mo-V steel, the effects of larger ripples (say R=0.85 and 0.80, which are relevant to TLP design) on the cracking resistance and the extent of ripple-load degradation on these steels are still lacking. Ripple load frequency, which is known to affect corrosion fatigue crack growth kinetics, should influence ripple load cracking time-to-failure curves, as indicated by Eq. 9.

5.0 Summary

- The presence of ripple loads can cause structural failure at a stress intensity significantly below the static K_{ISCC} threshold. To assure safety from the ripple effect, a new threshold parameter (K_{IRLC}) below which ripple-load cracking will not occur is identified and recommended as a design consideration if ripple-load conditions are suspected.

- TLP tendon pipe steel and 5Ni-Cr-Mo-V steel, which exhibit greater SCC resistance under static load conditions, are very susceptible to ripple-load degradation. On the other hand, SCC-susceptible high strength AISI 4340 steel display no damaging ripple-load effects.

- The extent of the ripple-load effect and K_{IRLC} depend on the size or the amplitude of the ripple. While a material may exhibit no ripple effect under a very small ripple loading, it may experience a substantial ripple-load degradation when subjected to a larger ripple loading condition.

- A predictive framework for the RLE has been developed from concepts and descriptors used in SCC and corrosion-fatigue characterization. Laboratory test results on both RLE-susceptible and nonsusceptible materials confirm the validity of the proposed framework.

- The critical conditions required for the appearance of a ripple-load effect have been defined.

- A mathematical expression has been developed to describe the maximum extent of ripple-load degradation for specific combinations of material/structure and loading conditions.

- A more efficient methodology for the establishment of time-to-failure curves for ripple-load cracking susceptible materials has been developed.

6.0 ACKNOWLEDGMENTS

The support of this work by the Minerals Management Service is gratefully acknowledged.

7.0 REFERENCES

1. *Stress-Corrosion Cracking in High Strength Steels and Aluminum and Titanium Alloys*, Edited by B.F. Brown, U.S. Government Printing Office, Washington, D.C. 1972.

2. M.O. Speidel, *Corrosion Fatigue of Steam Turbine Blade Materials*, (New York, NY: Pergamon, 1983), p. 1.

3. T.W. Crooker, J.A. Hauser II, and R.A.Bayles, "Ripple-Loading Effects on Stress-Corrosion Cracking in Steels," in *Proceedings of Third International Conference on Environmental Degradation of Engineering Materials - III*, Edited by Louthan, Jr., M.R., McNitt, R.P., and Sisson, Jr., R.D. , The Pennsylvania State University Press, University Park, PA, 1987, p. 521.

4. P.S. Pao, R.A. Bayles, and G.R. Yoder, "Effect of Ripple Load on the Stress-Corrosion Cracking in Structural Steels," in *Proceedings of 21st Annual OTC Conference*, Paper No. OTC 5983, Houston, TX, 1989, p. 245.

5. G.R. Yoder, P.S. Pao, and R.A. Bayles, "Ripple-Load Cracking in a Titanium Alloy," Scripta Met. 24(1990), p. 2285.

6. P.S. Pao, S.J. Gill, R.A. Bayles, and G.R. Yoder, "Effect of Ripple Loads on Stress-Corrosion Cracking in Al 7075 Alloys," Scripta Met. 25(1991), p. 2085.

7. P.S. Pao, D.A. Meyn, R.A. Bayles, C.R. Feng, and G.R. Yoder, "Effect of Ripple Loads on Sustained-Load Cracking in Titanium Alloys," to be published in Scripta Met. (1995).

8. P.S. Pao, D.A. Meyn, R.A. Bayles, C.R. Feng, and G.R. Yoder, "On Ripple-Load, Stress-Corrosion, and Sustained-Load Cracking Behavior in a High Strength Beta Titanium Alloy," submitted to Scripta Met.

9. R.N. Parkins, and B.S. Greenwell, "The Interface Between Corrosion Fatigue and Stress-Corrosion Cracking," Metal Science, Aug./Sept. 1977, pp. 405-413.

10. R.N. Parkins, P.M. Singh, "Stress Corrosion Crack Coalescence," Corrosion 46(1990), p. 485.

11. K. Endo, and K. Komai, "Effects of Stress Wave Form and Cycle Frequency on Low Cycle Corrosion Fatigue," in *Corrosion Fatigue: Chemistry, Mechanics, and Microstructure, NACE-2*, Edited by O.F. Devereax, A.J. McEvily, and R.W. Staehle, NACE, Houston, 1972, pp. 437-450.

12. K. Endo and K. Komai, "Influences of Secondary Stress Fluctuations of Small Amplitude on Low-Cycle Corrosion Fatigue," in *Corrosion Fatigue Technology, ASTM STP 642*, Edited by H.L. Craig, Jr., T.W. Crooker, and D.W. Hoeppner, ASTM, Philadelphia,1978, pp. 74-97.

13. K. Endo, K. Komai, and M. Himejima, Trans. Japan Soc. Mech. Engrs. 37(1971), p. 2036.

14. K. Endo, K. Komai, and N. Imashiro, Trans. Japan Soc. Mech. Engrs. 42(1976), p. 2652.

15. K. Komai, K. Minoshima, H. Yukimachi, "The Influence of Temperature on Static and Dynamic SCC Crack Growth Behavior in Aluminum Alloy," Japan Congr. Mater. Res. 20(1984), p. 57.

16. F.P. Ford and M. Silverman, "The Effect of Loading Rate on Environmentally Controlled Cracking of Sensitized 304 Stainless Steel in High Purity Water," Corrosion-NACE, Vol. 36, No. 11, Nov. 1980, pp. 597-603.

17. J. Mendoza and J.M. Sykes, "The Effect of Low-Frequency Cyclic Stresses on the Initiation of Stress Corrosion Cracks in X60 Line Pipe Steel in Carbonate Solutions," Corrosion Science, Vol. 23, No. 6, 1983, pp. 547-558.

18. R.R. Fessler and T.J. Barlo, "Threshold-Stress Determination Using Tapered Specimens and Cyclic Stresses," in *Environment-Sensitive Fracture: Evaluation and Comparison of Test Methods, ASTM STP 821*, Edited by S.W. Dean, E.N. Pugh, and G.M. Ugiansky, ASTM, Philadelphia, 1984, pp. 368-382.

19. R.W. Judy, Jr., W.E. King, Jr., J.A. Hauser II, and T.W. Crooker, "Influence of Environmental Variables on the Measurement of Stress-Corrosion Cracking Properties of High-Strength Steels," NRL Memorandum Report 5896, Naval Research Laboratory, Washington, D.C., 1986.

20. R.W. Hertzberg, "*Deformation and Fracture Mechanics of Engineering Materials*," Wiley, New York, 1983.

21. O. Vosikovsky, "Frequency, Stress Ratio, and Potential Effects on Fatigue Crack Growth on HY130 Steel in Salt Water," J. Testing and Evaluation, Vol. 6, No. 3, 1978, pp. 175-182.

22. R.P. Wei and J.D. Landes, "Correlation Between Sustained Load and Fatigue Crack Growth in High Strength Steels," Materials Research and Standards, Vol. 9, No. 7, 1969, pp. 25-28.

23. R.P. Gangloff and J.R. Scully, Annual Research Report "Environmentally Assisted Cracking of High Strength Beta Titanium Alloys", SEAS Report No. UVA/525464/MSE93/101, University of Virginia, Charlottesville, VA, 1992.

24. J.K. Donald and D.W. Schmidt, "Computer-Controlled Stress Intensity Gradient Technique for High Rate Fatigue Crack Growth Testing," J. Testing and Evaluation, Vol. 8, No. 1, May 1980, pp. 19-24.

TABLE 1 - CHEMICAL COMPOSITIONS (Weight percent)

Material	C	Mn	P	S	Si	Cu	Ni	Cr	Mo	V
5Ni-Cr-Mo-V	0.13	0.82	–	0.002	0.24	0.05	5.20	0.44	0.52	0.05
4340	0.14	0.74	0.01	0.016	0.21	–	2.0	0.74	0.26	0.05
TLP Tendon Pipe	0.06				0.2	0.21	0.2			

TABLE 2 - TENSILE PROPERTIES

Material	0.2% Yield Strength, MPa (ksi)	Ultimate Tensile Strength, MPa (ksi)	Elongation in 2-in., %	Reduction in Area, %
5Ni-Cr-Mo-V	965 (140)	1,014 (147)	–	–
4340	1,207 (175)	1,282 (186)	25	11
TLP Tendon Pipe	448 (65)	545 (79)	45	

TABLE 3 - PREDICTED AND MEASURED THRESHOLD VALUES (MPa√m)

		TLP Steel	5Ni-Cr-Mo-V Steel			4340 Steel
		R=0.90	R=0.90	R=0.95	R=0.975	R=0.90
ΔK_{th}		3.15	3.1	2.95	2.875	3.3
K_{IRLC}	Predicted	31.5	31	59	115	33
	Measured*	-	44	80	110	33
K_{ISCC}		78**	110			33

* BASED ON 4000-HOUR TESTS.

** ESTIMATED.

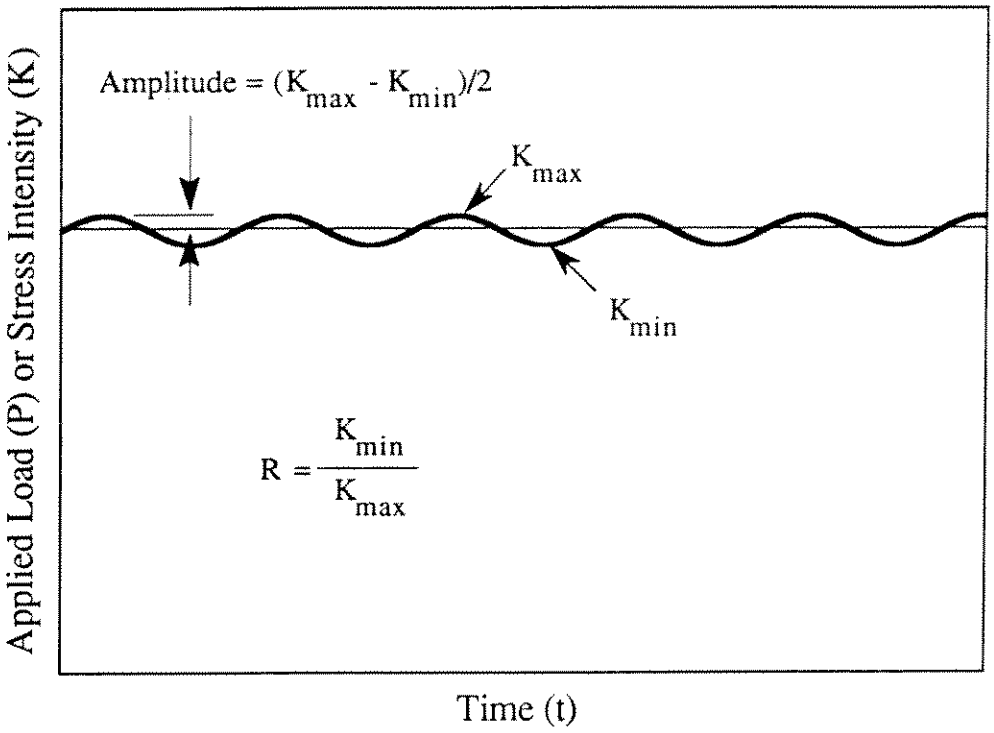

Figure 1. A ripple-load profile.

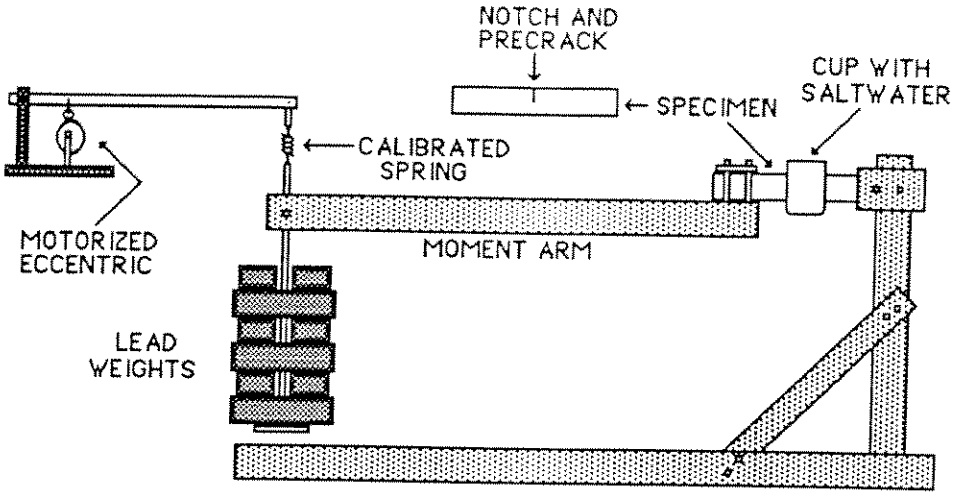

Figure 2. Ripple-load "direct experiment".

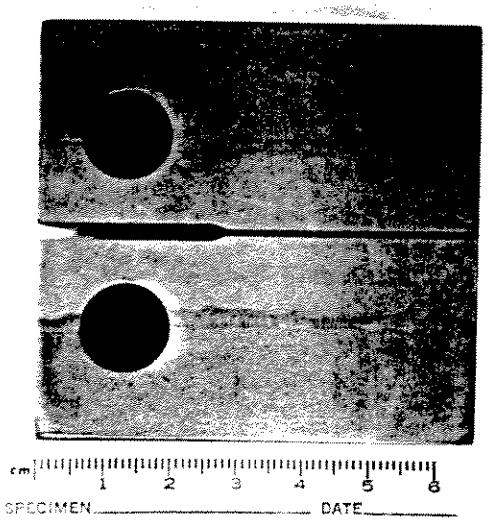

Figure 3. Ripple-load cracking test specimen from the weld region.

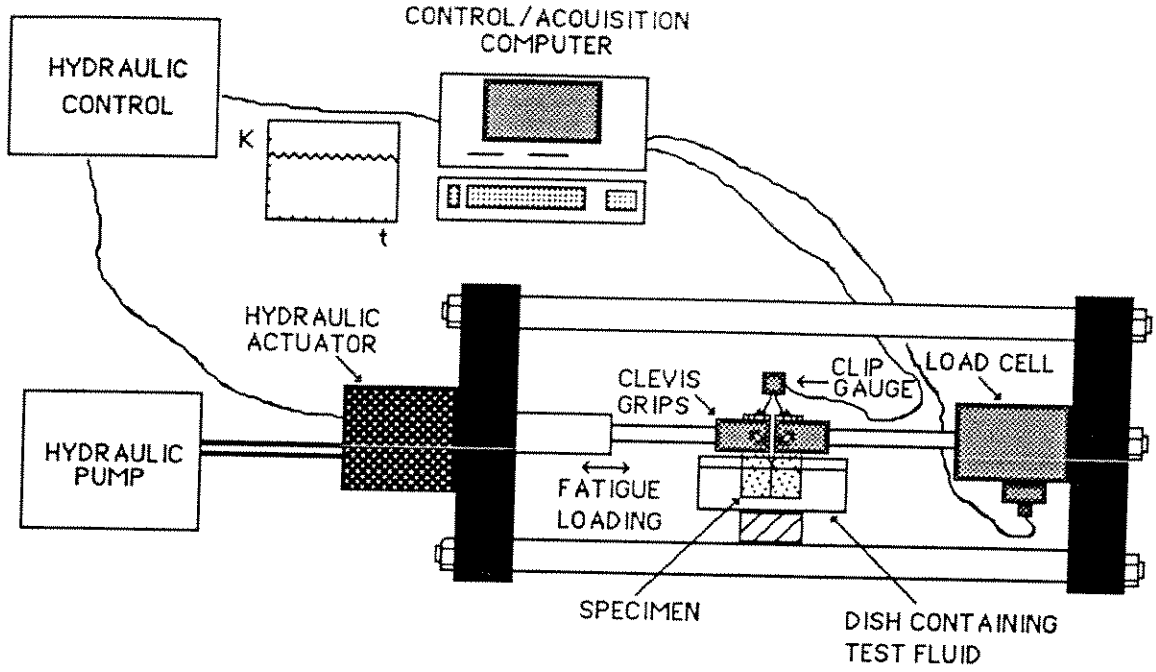

Figure 4. Corrosion-fatigue test machine.

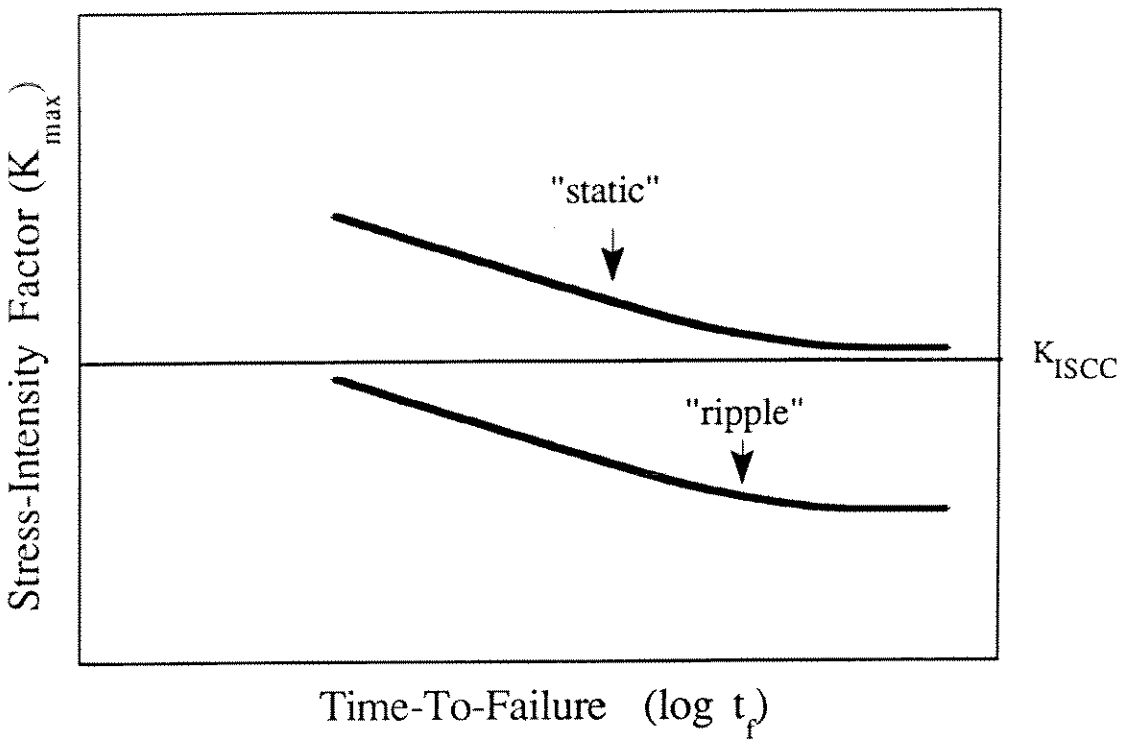

Figure 5. Schematic showing the ripple-load effect.

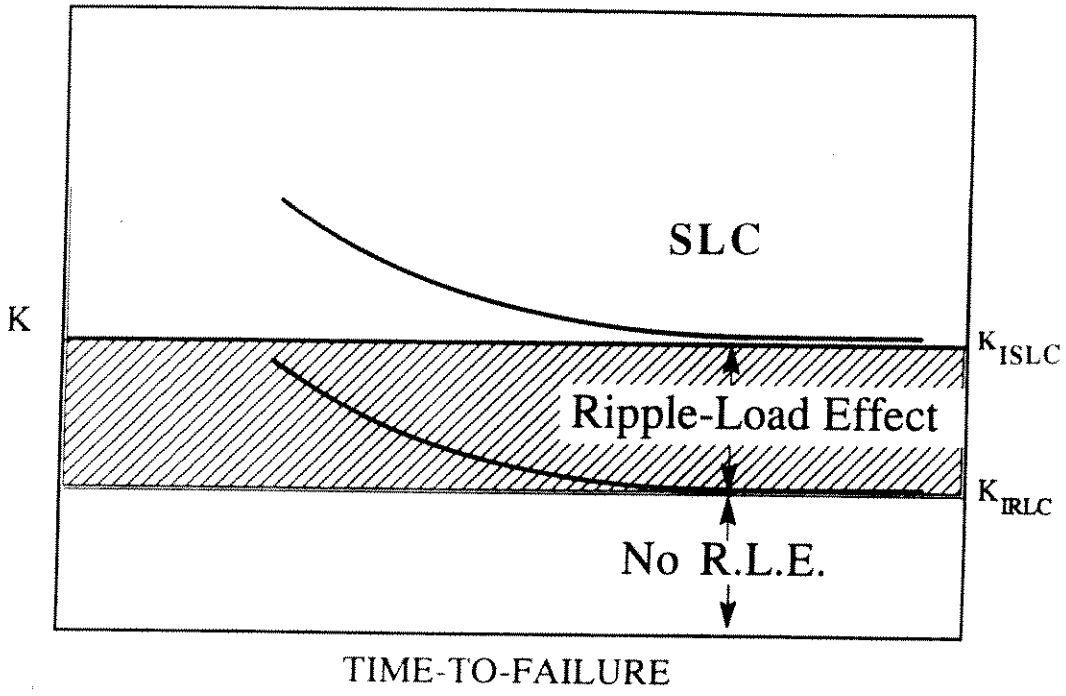

Figure 6. Schematic showing the ripple-load effect and the "window of susceptibility".

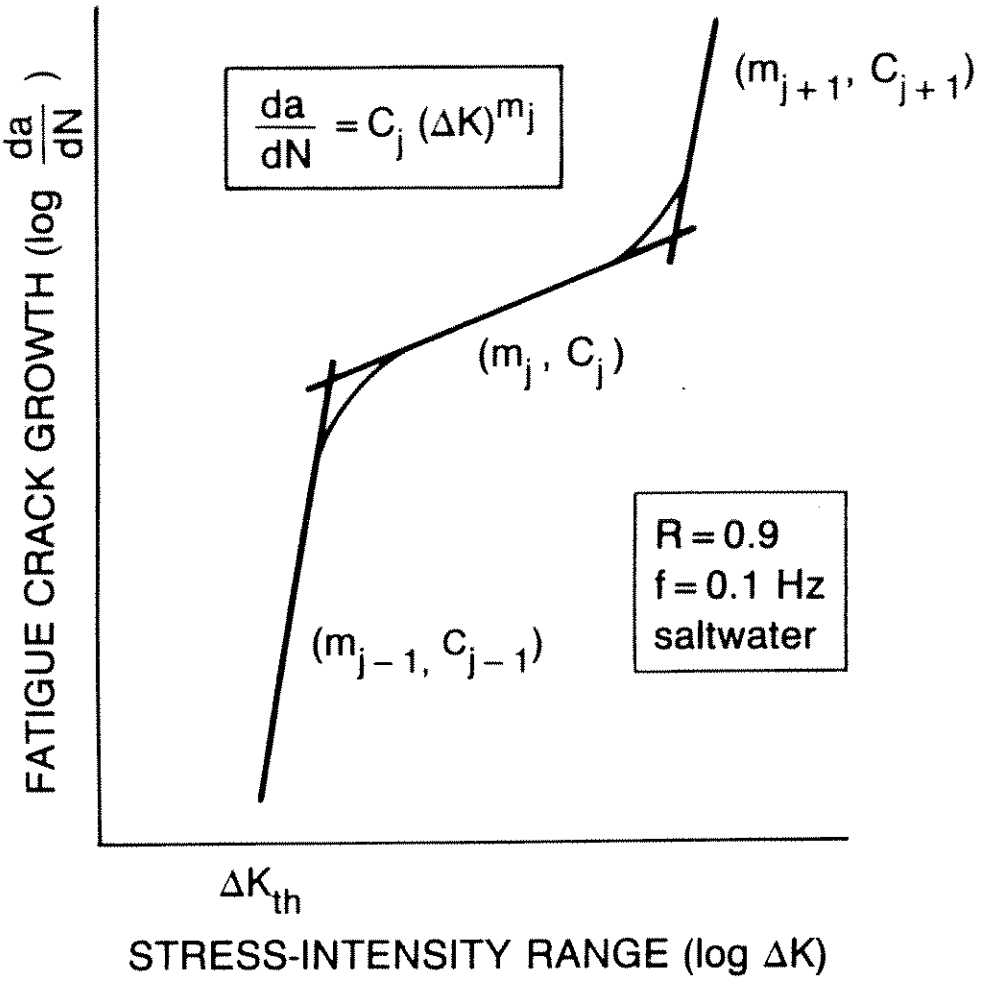

Figure 7. Piecewise analysis of corrosion-fatigue crack growth rate curve via power-law approximation to j^{th} segment.

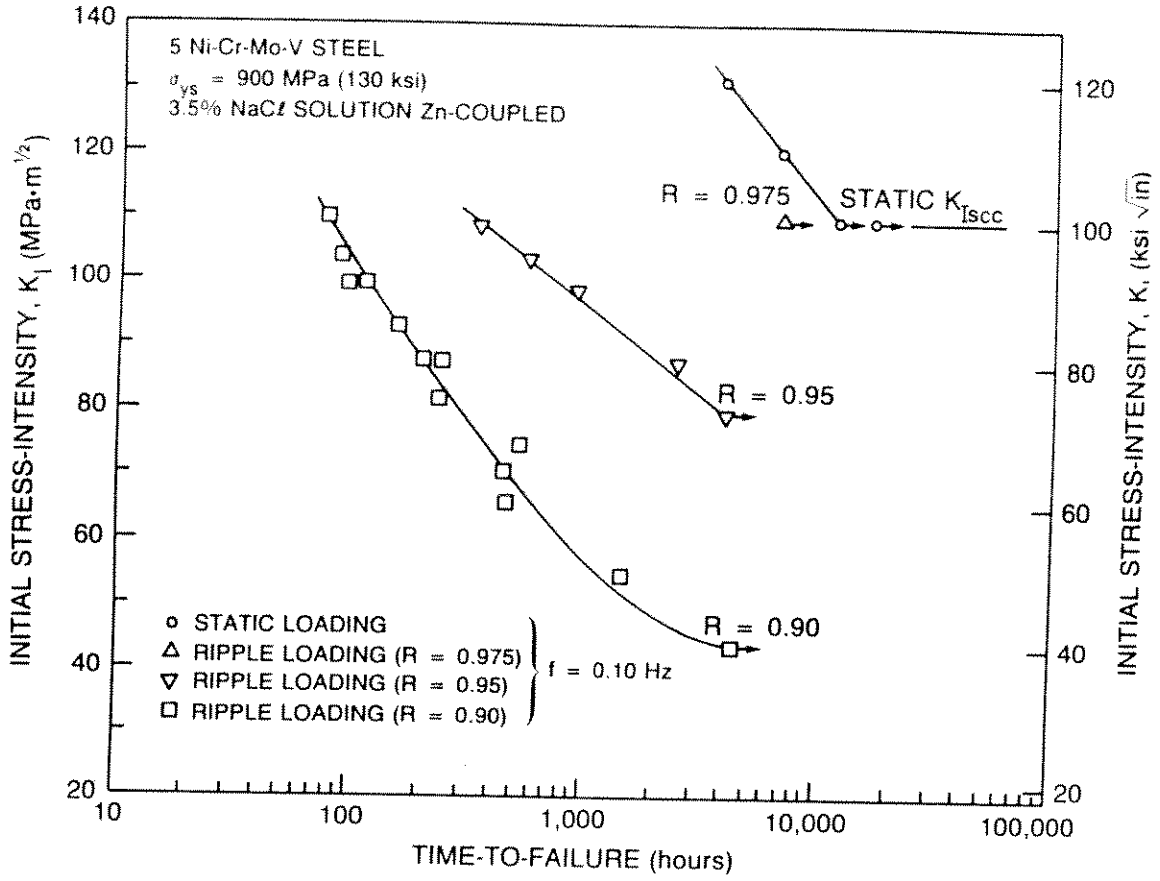

Figure 8. Initial stress-intensity (K_I) versus time-to-failure data for 5Ni-Cr-Mo-V steel under static loading and ripple-loading.

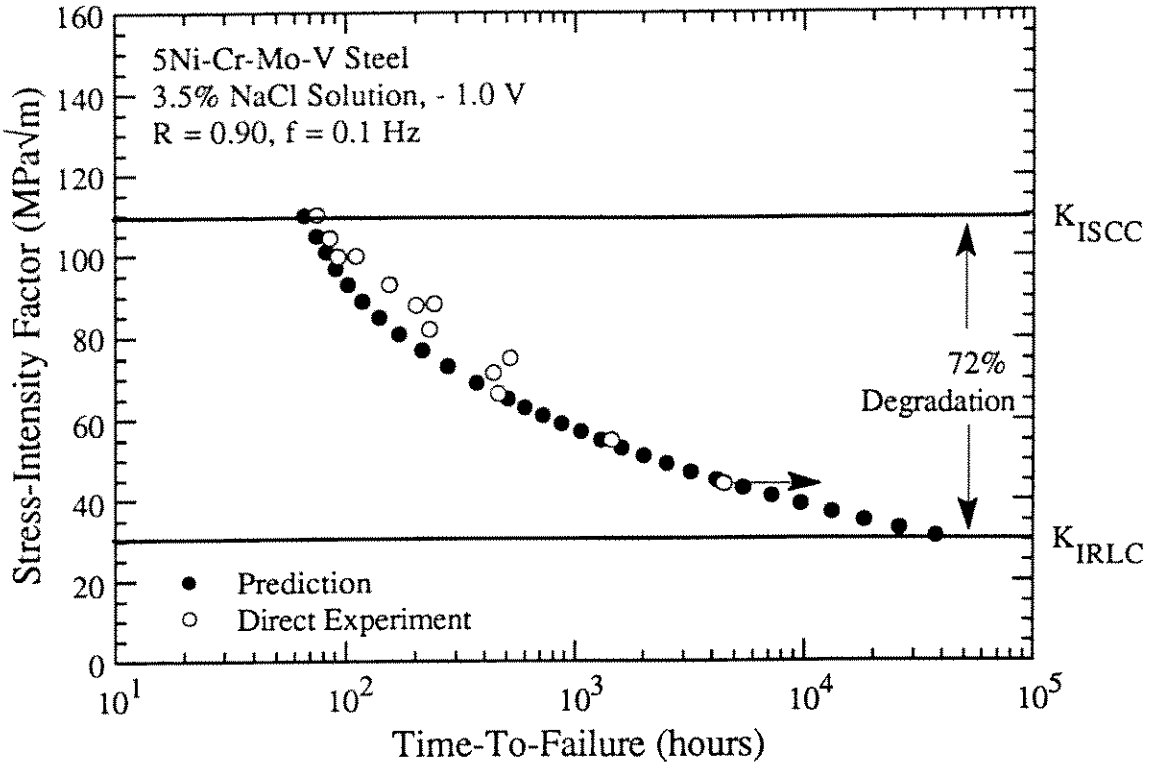

Figure 9. Comparison of the predicted time-to-failure curve obtained through integration of fatigue data to laboratory data for 5Ni-Cr-Mo-V steel under ripple-loading condition (R=0.90).

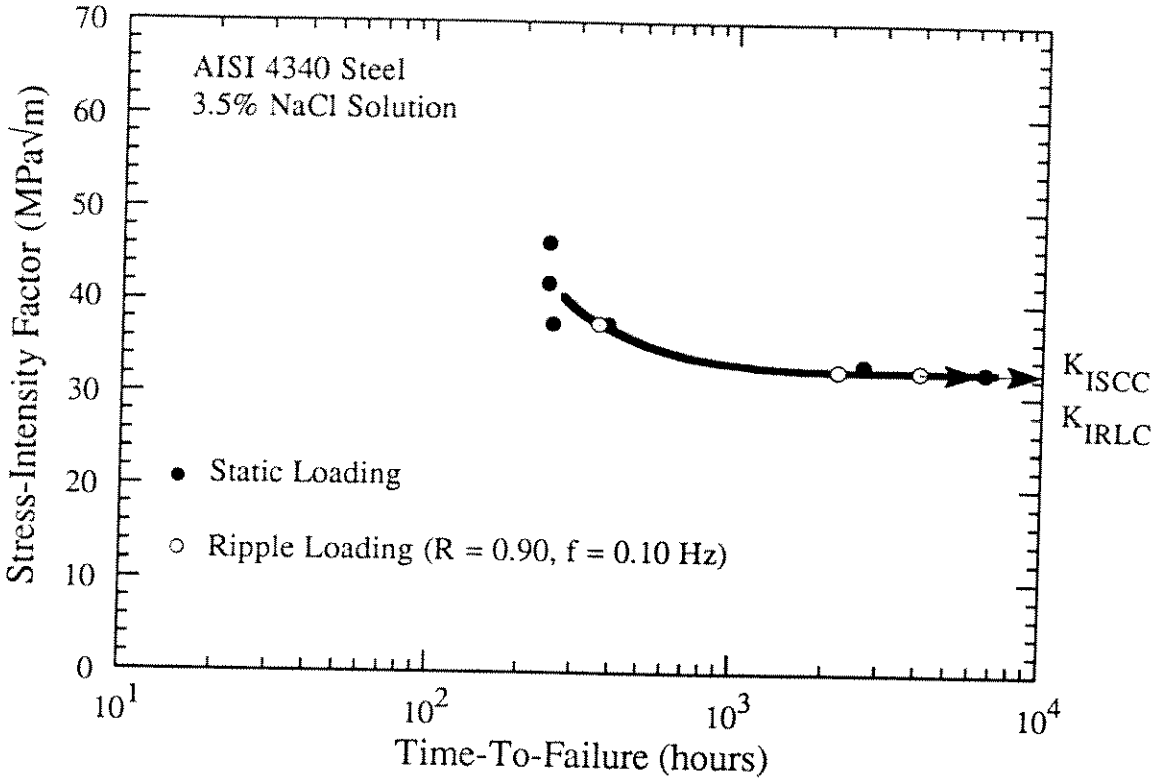

Figure 10. Initial stress-intensity (K_I) versus time-to-failure data for high strength AISI 4340 steel under static loading and ripple-loading (R=0.90).

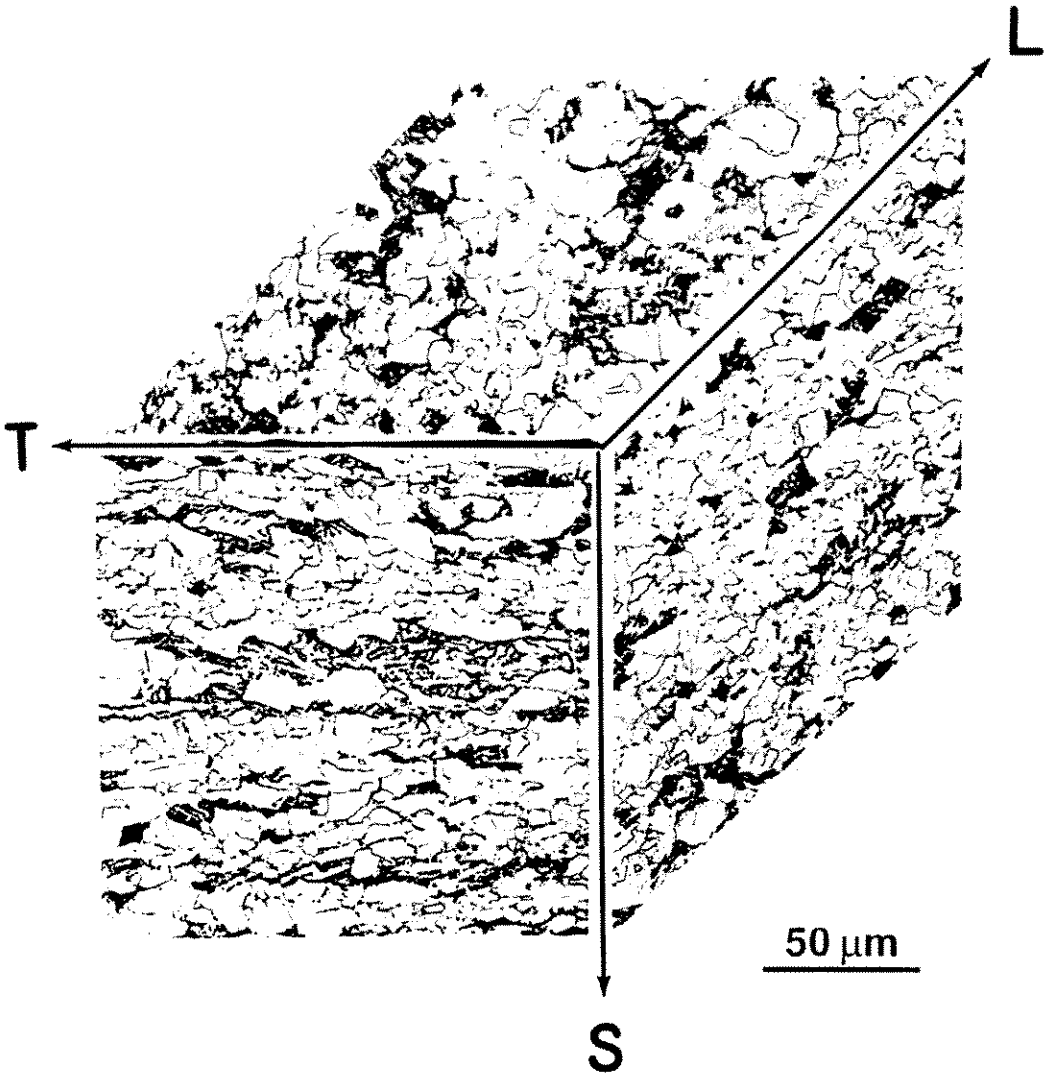

Figure 11. Microstructure of the base metal for TLP tendon pipe steel.

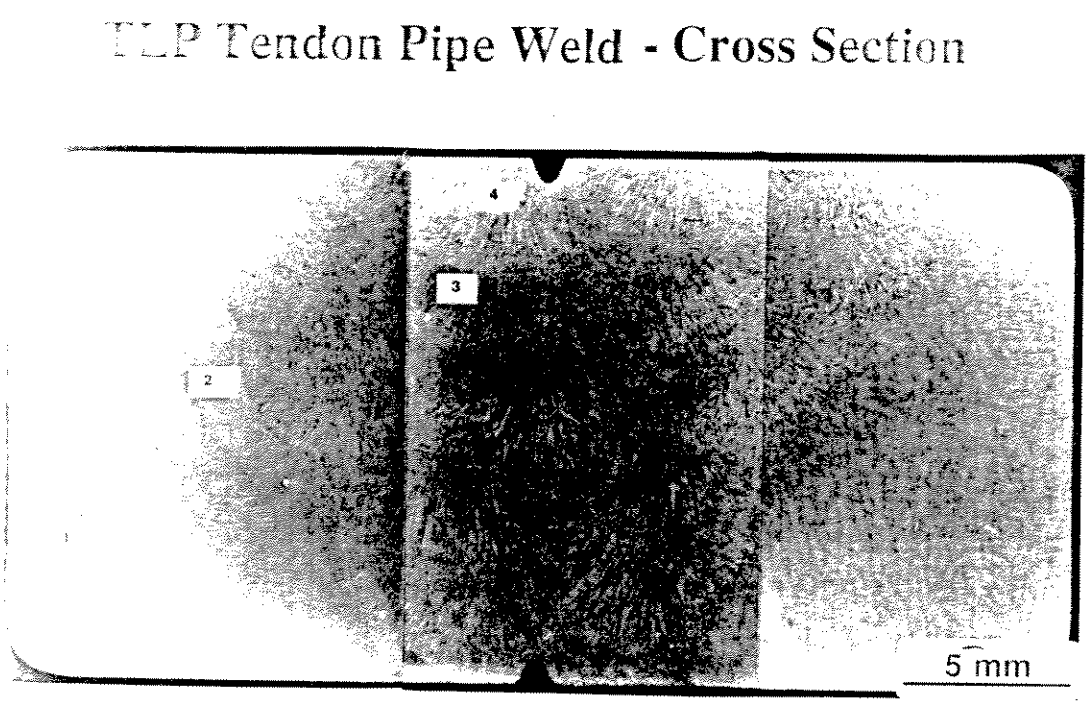

Figure 12. Microstructure of the weld region for TLP tendon pipe steel.

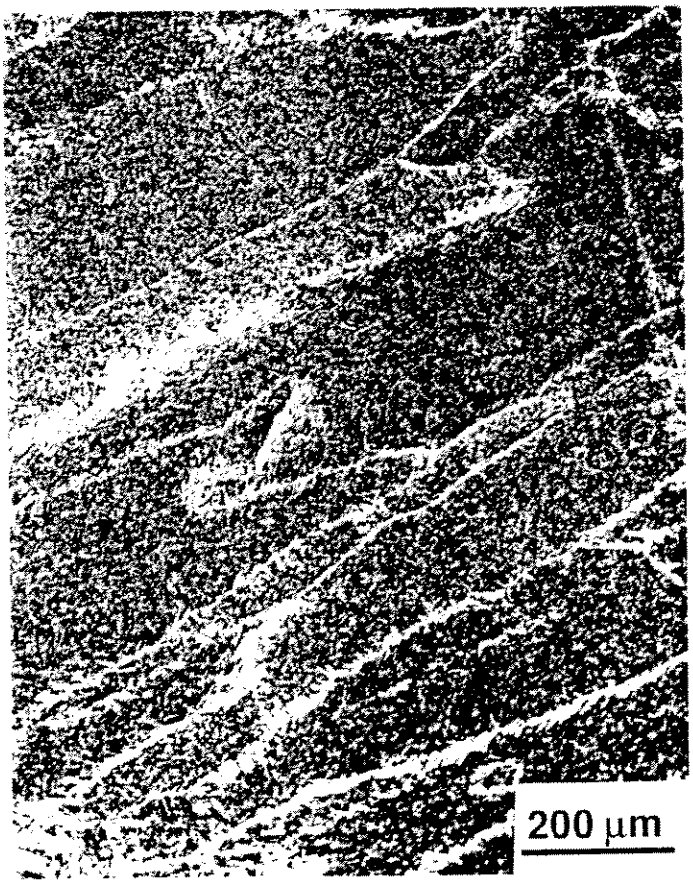

Figure 13. Large columnar grains in the fusion zone.

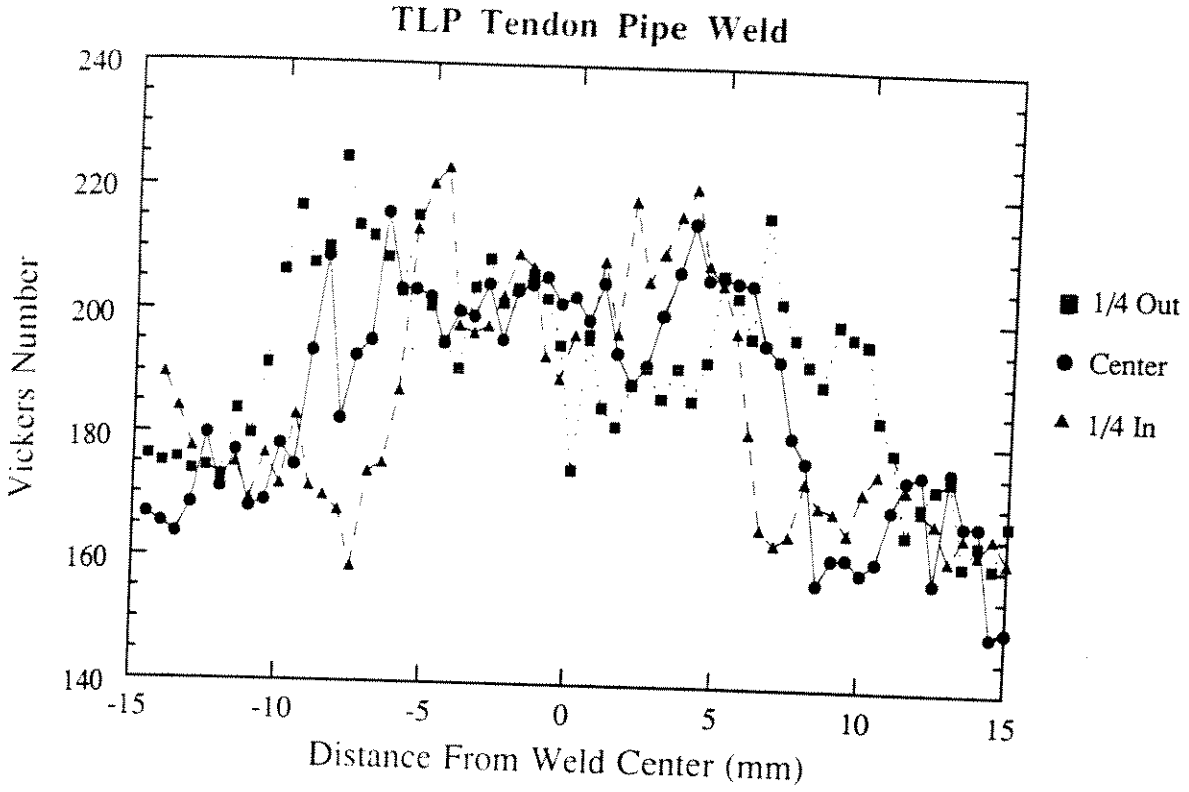

Figure 14. The microhardness across the weld of TLP tendon pipe steel.

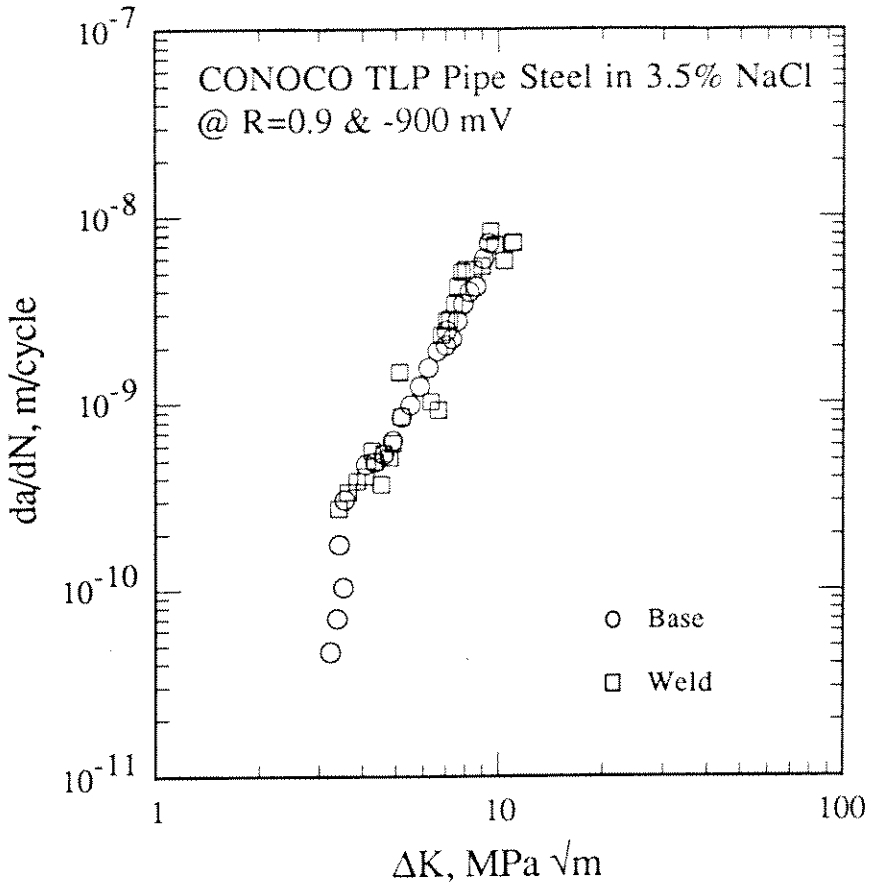

Figure 15. Fatigue crack growth in the base metal and weld region for TLP tendon pipe steel in a 3.5% NaCl solution at R=0.90.

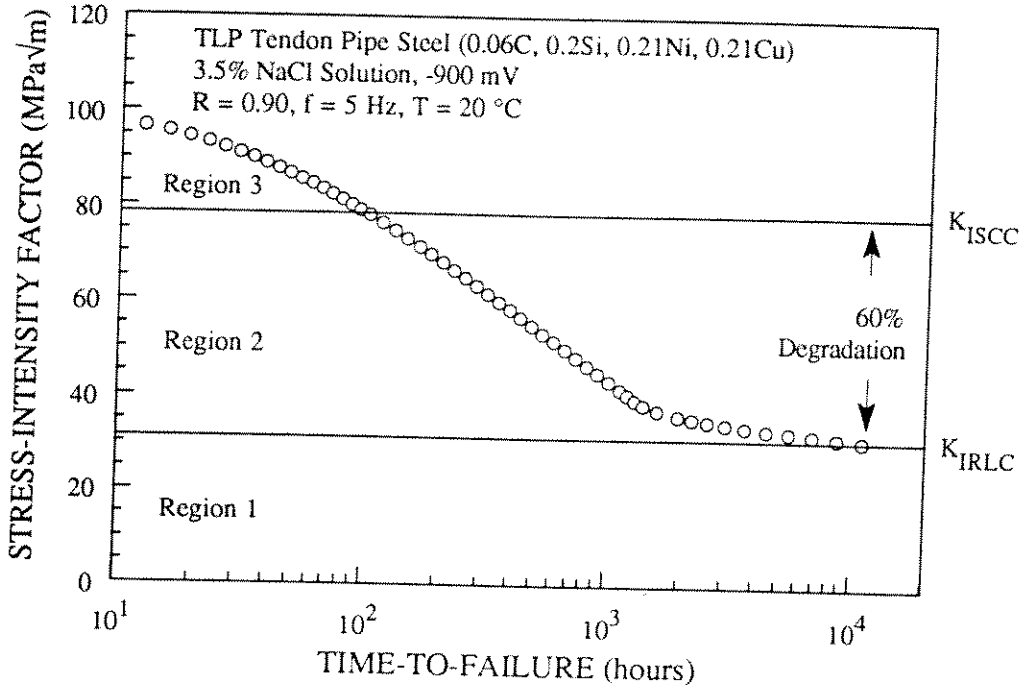

Figure 16. Predicted time-to-failure curve obtained through integration of base metal fatigue data at 20 °C for TLP tendon pipe steel under ripple-loading condition (R=0.90).

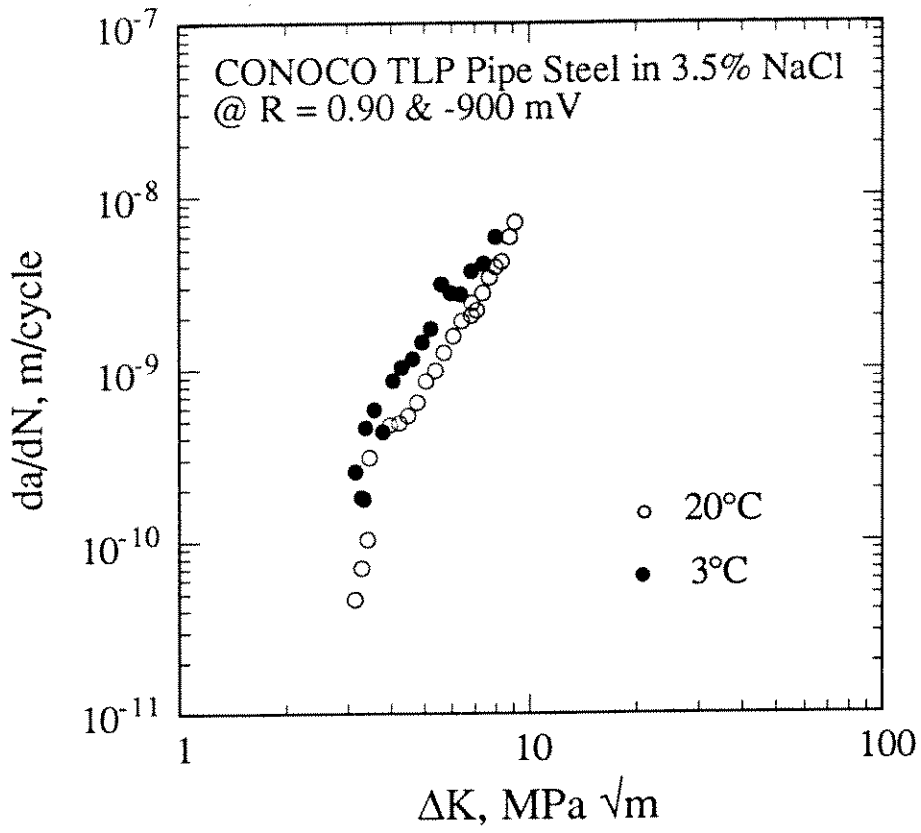

Figure 17. Fatigue crack growth of the base metal at 3 °C and 20 °C for TLP tendon pipe steel in a 3.5% NaCl solution at R=0.90.

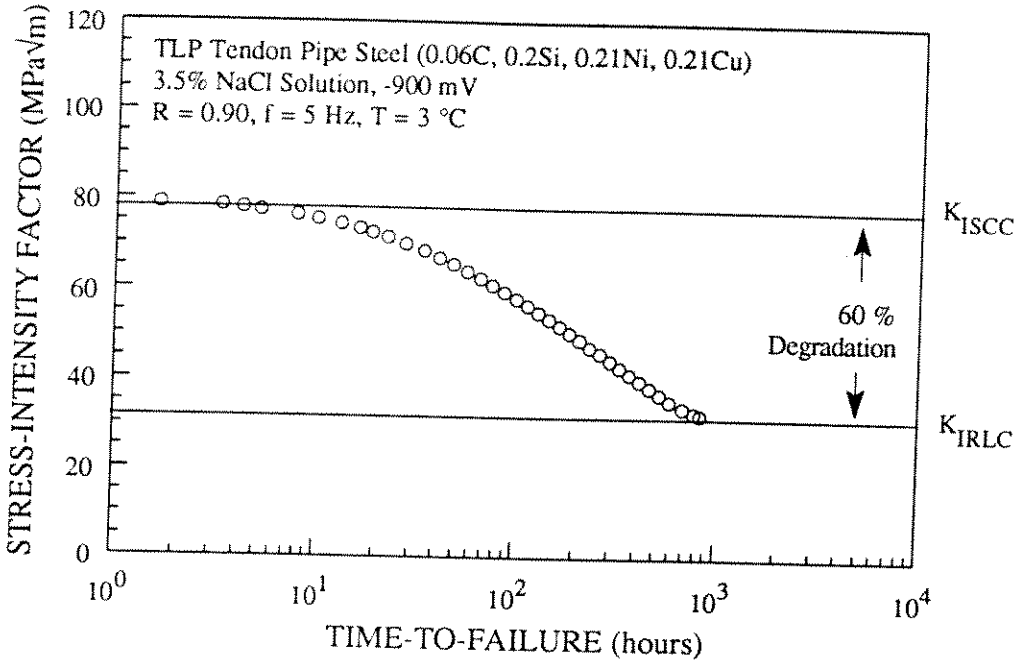

Figure 18. Predicted time-to-failure curve obtained through integration of base metal fatigue data at 3 °C for TLP tendon pipe steel under ripple-loading condition (R=0.90).

Figure Captions

Figure 1. A ripple-load profile.

Figure 2. Ripple-load "direct experiment".

Figure 3. Ripple-load cracking test specimen from the weld region.

Figure 4. Corrosion-fatigue test machine.

Figure 5. Schematic showing the ripple-load effect.

Figure 6. Schematic showing the ripple-load effect and the "window of susceptibility".

Figure 7. Piecewise analysis of corrosion-fatigue crack growth rate curve via power-law approximation to j^{th} segment.

Figure 8. Initial stress-intensity (K_I) versus time-to-failure data for 5Ni-Cr-Mo-V steel under static loading and ripple-loading.

Figure 9. Comparison of the predicted time-to-failure curve obtained through integration of fatigue data to laboratory data for 5Ni-Cr-Mo-V steel under ripple-loading condition (R=0.90).

Figure 10. Initial stress-intensity (K_I) versus time-to-failure data for high strength AISI 4340 steel under static loading and ripple-loading (R=0.90).

Figure 11. Microstructure of the base metal for TLP tendon pipe steel.

Figure 12. Microstructure of the weld region for TLP tendon pipe steel.

Figure 13. Large columnar grains in the fusion zone.

Figure 14. The microhardness across the weld of TLP tendon pipe steel.

Figure 15. Fatigue crack growth in the base metal and weld region for TLP tendon pipe steel in a 3.5% NaCl solution at R=0.90.

Figure 16. Predicted time-to-failure curve obtained through integration of base metal fatigue data at 20 °C for TLP tendon pipe steel under ripple-loading condition (R=0.90).

Figure 17. Fatigue crack growth of the base metal at 3 °C and 20 °C for TLP tendon pipe steel in a 3.5% NaCl solution at R=0.90.

Figure 18. Predicted time-to-failure curve obtained through integration of base metal fatigue data at 3 °C for TLP tendon pipe steel under ripple-loading condition (R=0.90).